On the Stability of the Soluble Amyloid Aggregates

Bankanidhi Sahoo,[†] Suman Nag,[†] Parijat Sengupta,[‡] and Sudipta Maiti[†*]
[†]Department of Chemical Sciences, Tata Institute of Fundamental Research, Colaba, Mumbai, India; and [‡]Program in Neuroscience, Department of Veterinary and Comparative Anatomy, Pharmacology, and Physiology, Washington State University, Pullman, Washington

ABSTRACT Many amyloid proteins form metastable soluble aggregates (or protofibrils, or protein nanoparticles, with characteristic sizes from ~10 to a few hundred nm). These can coexist with protein monomers and amyloid precipitates. These soluble aggregates are key determinants of the toxicity of these proteins. It is therefore imperative to understand the physical basis underlying their stability. Simple nucleation theory, typically applied to explain the kinetics of amyloid precipitation, fails to predict such intermediate stable states. We examine stable nanoparticles formed by the Alzheimer's amyloid-β peptide (40 and 42 residues), and by the protein barstar. These molecules have different hydrophobicities, and therefore have different short-range attractive interactions between the molecules. We also vary the pH and the ionic strength of the solution to tune the long-range electrostatic repulsion between them. In all the cases, we find that increased long-range repulsion results in smaller stable nanoparticles, whereas increased hydrophobicity produces the opposite result. Our results agree with a charged-colloid type of model for these particles, which asserts that growth-arrested colloid particles can result from a competition between short-range attraction and long-range repulsion. The nanoparticle size varies superlinearly with the ionic strength, possibly indicating a transition from an isotropic to a linear mode of growth. Our results provide a framework for understanding the stability and growth of toxic amyloid nanoparticles, and provide cues for designing effective destabilizing agents.

INTRODUCTION

Amyloid aggregation of proteins is linked to various neurodegenerative diseases (1–5). The aggregation intermediates, from dimers to the larger soluble aggregates, are thought to significantly contribute to the toxicity of these amyloid proteins. The relative toxicity contributions of the different types of aggregates is still far from clear, but the soluble aggregates (protofibrils or nanoparticles, $>$10 nm in size) are suspected to be substantial contributors, e.g., in the case of amyloid-β (which causes Alzheimer's disease) (6–12). Indeed, it has been shown that chemical agents (such as Zn^{2+}) which can destabilize these nanoparticles also reduce the toxicity of the peptides (7,13). Therefore, understanding the mechanism that ensures the stability of the nanoparticles can provide directions for designing agents that can destabilize them.

However, understanding this mechanism remains a significant unsolved problem. Simple nucleation theories suggest that postnucleation particles should continue to grow indefinitely in a saturated solution (14,15). The existence of a well-defined saturation concentration, which is a thermodynamic precondition for nucleation-mediated aggregation, has been established (16). There is also ample evidence that the aggregation of many of the common amyloid proteins occur via a nucleation process (17,18). The size of this nucleus is thought to be of approximately a few nm (11,19,20). The lag-phase observed during the initial growth agrees with the kinetics predicted by this model (17). Even the dependence of the kinetics on supersaturation is well established, and useful bounds for parameters such as the surface energy have been estimated from these measurements (19).

Although the existence of a post-nucleation stable state is not predicted by the nucleation theory, metastable aggregates of size 10 nm or larger are regularly found in an aggregating solution (7,13). These bear similarity to the growth-arrested colloid particles, which has been a system of recent interest (21,22). Charged colloid particles can be stabilized by a competition between short-range attractive and long-range repulsive interactions (22). Small but stable lysozyme aggregates (consisting of a few monomers), have been observed in small angle neutron scattering experiments, and are suggested to have the same origin as that of charged colloid clusters (23). Though the inference regarding the lysozyme aggregates have been debated (24), and the nanoparticles investigated here are much larger, this suggests that a competition between short-range attraction and long-range repulsion may also be important in determining the stability of the amyloid aggregates. Such a model would predict that as a nanoparticle grows and the charge on it increases, the electrostatic repulsion between the particle and an approaching monomer increases. As the particle grows to a certain characteristic size (and thus a sufficiently high charge), this repulsion becomes large enough to drastically slow further growth. However, the short-range attraction remains strong enough to assimilate a monomer if it can come within a short distance of the particle. The particles of this characteristic size thus become metastable.

For the amyloid aggregates, we can independently vary the two competing interactions, and can simultaneously measure their effect on the size and the stability of the soluble aggregates. The model predicts that if the average charge per

Submitted January 1, 2009, and accepted for publication May 20, 2009.

*Correspondence: maiti@tifr.res.in

Editor: Elliot L. Elson.

0006-3495/09/09/1454/7 $2.00

doi: 10.1016/j.bpj.2009.05.055

monomer is increased (which can be achieved by moving away from the iso-electric point (pI) of the protein), or the electrostatic screening by the aqueous solution is decreased (which can be achieved by reducing the ionic strength), the nanoparticle should reach stability at a smaller size. On the other hand, if the hydrophobicity of the aggregating protein increases, in effect increasing the short-range interaction, the characteristic size should increase. If the characteristic size is beyond a certain limit, these particles will precipitate from the aqueous solution, in effect leaving the solution void of any stable nanoparticles. The hydrophobic interactions can be varied by introducing specific hydrophobic residues, or by creating the molten globule state of a suitable protein using denaturants (for those proteins for which such a state exists). This serves as a handle to tune the short-range attraction. The particle sizes can be measured by using fluorescence correlation spectroscopy (FCS) (25,26), employing the maximum entropy method-based analysis routine MEMFCS (27), as demonstrated by us previously (16,19).

Here we study the soluble aggregates formed by Alzheimer's amyloid beta 1-40 ($A\beta_{1\text{-}40}$) and 1-42 ($A\beta_{1\text{-}42}$) peptides. Both of these are known to cause neuropathologies, and they differ by only two extra residues contained in $A\beta_{1\text{-}42}$, such as Ile^{41} and Ala^{42}. From the sequence, it appears likely that the pI of the two peptides would be similar, but $A\beta_{1\text{-}42}$ would be more hydrophobic. With the given model, we therefore expect that the $A\beta_{1\text{-}40}$ should form smaller-sized soluble aggregates. These $A\beta_{1\text{-}40}$ aggregates have in fact been characterized by us in previous experiments, and their hydrodynamic radii range from tens to hundreds of nm (7,13,16). If the aggregates of $A\beta_{1\text{-}42}$ are much bigger than this, they would not be soluble, and would precipitate out of the solution in due course.

We also study the aggregates formed by the protein barstar. Barstar is a 10-kDa protein produced in *Bacillus amyloliquefaciens* as a ribonuclease inhibitor and is not related to any known diseases, but is known to form amyloid aggregates at a low pH (28–30). Barstar changes its folding pattern with pH (31), forming a molten globule like state at pH values at ~3. The pI of barstar is ~5.0 (32,33). This provides a unique opportunity to test the charged colloid model. At physiological pH, barstar is folded to a native state with well-buried hydrophobic residues. At approximately pH 3.5, partial unfolding results in exposed hydrophobic patches. The degree of hydrophobicity can be quantified by the fluorescence of the reporter dye ANS. At even lower pH (<3), these hydrophobic patches start to disappear, as the protein unfolds further. In addition, the protein becomes increasingly positively charged. The charged colloid model would predict that the soluble aggregates would start forming as we go down from pH 7.4 to 3.5. However, as we move below this pH, the aggregate sizes should start to reduce.

We test these predictions by determining the stability and the size of the soluble aggregates using fluorescence correlation spectroscopy (34–36).

THEORY

We consider a heuristic model for understanding the dependence of the size of the quasistable nanoparticle on the attractive and repulsive interactions in the system. For simplicity, we presume that when a protein nanoparticle grows in a supersaturated solution, the attractive interaction is solely provided by short-range hydrophobic interaction. Although an accurate analytical description of the hydrophobic interaction as a function of distance is not available, it is known that the major part of the interaction occurs at a length scale of <1 nm (37). It is reasonable to assume that the spatial scale is set by the thickness of a water layer (~0.2 nm), over which the density of water near a nonpolar particle varies from its bulk density (38). We also assume that the repulsive interaction is provided by electrostatic interaction between the growing nanoparticle and an approaching monomer. The length scale of the repulsion is set by the Debye screening length of the electrolyte solution (39), which is ~0.8 (2.5) nm in the highest (lowest) ionic strength solution reported here. Thus the range of the repulsive interaction remains large compared to the range of the attractive interaction, and we approximate the hydrophobic interaction by a negative step function extending up to the radius of the particle a (though this assumption starts becoming inappropriate for the highest ionic strengths). This is shown as a black dotted line in Fig. 1.

The rate of growth of a solute nanoparticle in a supersaturated solution is determined by the concentration of

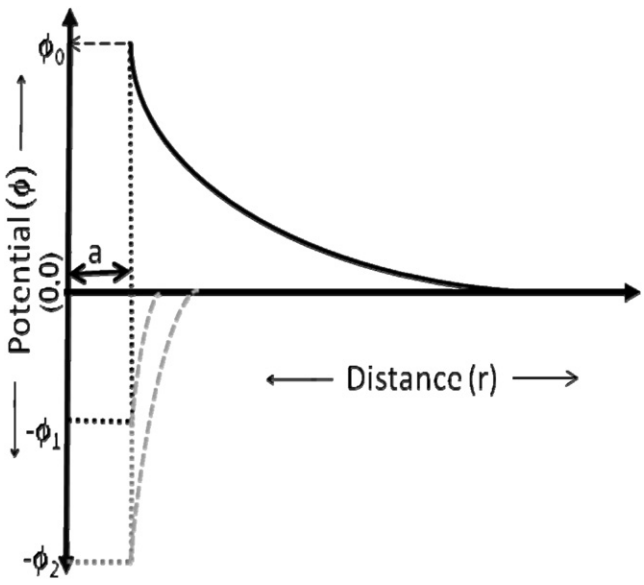

FIGURE 1 Model potential function. The model consists of a repulsive electrostatic potential screened by the ionic solution (*solid line*) and an attractive hydrophobic potential (step function, *black dotted line*), which are plotted here as functions of distance r from the center of the nanoparticle of radius a. The value ϕ_0 is the maximum height of the potential, whereas ϕ_1 is the minimum of the potential. If the range of the attractive potential is not infinitesimally short (e.g. see the *gray dotted lines*), ϕ_0 will change as the depth of the potential changes from ϕ_1 to ϕ_2.

monomers available at its surface, which for a given bulk concentration is determined by the electrostatic potential at the surface of the nanoparticle (ϕ in Fig. 1). This assumes that the monomer concentration near the accreting nanoparticle remains close to its bulk value. This is a reasonable assumption provided the growth rate is sufficiently slow.

The concentration of the monomers $C(a)$ at the surface of a nanoparticle of radius a is given as

$$C(a) = C_\infty e^{-\phi(a)q/kT}, \quad (1)$$

where C_∞ is the bulk concentration of monomers, q is the charge of a monomer unit, k is the Boltzmann constant, T is the temperature of the system, and $\phi(a)$ is the electrostatic potential at the surface of the nanoparticle, which in an ionic solution is given as (39,40)

$$\phi(a) = Zq/\varepsilon a(1 + \kappa a), \quad (2)$$

where Z is the total number of monomers constituting the nanoparticle, ε is the dielectric constant of the medium, and κ is the screening parameter, defined as

$$\kappa = \left(8\pi N_0 q^2 I/1000\varepsilon kT\right)^{1/2}. \quad (3)$$

Here N_0 is the Avogadro's number and I is the ionic strength of the solution in moles/L, whereas other quantities are in cgs units.

The total number of monomers Z in the nanoparticle is given by

$$Z = a^3/a_0^3, \quad (4)$$

where a_0 is the radius of an individual monomer unit. Therefore to obtain the same repulsive potential, ϕ_a on the surface of nanoparticles at different ionic strengths, Eqs. 2–4 implies (assuming $\kappa a \gg 1$, true for experiments described here)

$$a \propto I^{1/2}. \quad (5)$$

As the particle grows, the total number of charged monomers (Z) on the nanoparticle no longer grows as a^3, since the free energy cost of burying a charge inside a hydrophobic particle is rather high. In the limit, when a becomes large, and if the particle is reasonably compact with a water-inaccessible core, Z would vary as a^2. Alternatively, the particle can also grow linearly (i.e., as a cylinder) and not spherically, which would also make Z proportional to a^2. In that limit, a becomes independent of I. We therefore expect to see a transition between a growing as $I^{1/2}$ at small ionic strengths, to a, becoming independent of I at large ionic strengths. This would manifest as a sublinear to a superlinear transition in the dependence of a on I in the intermediate range of ionic strengths.

This model can also be used to understand the effect of pH on the radius of a stable nanoparticle. At a given ionic strength, q increases as we move away from the pI of the peptide. Therefore, the same electrostatic potential ϕ_0 will now be formed at a smaller size of the nanoparticle, as evident from Eqs. 2 and 4.

In this approximation, the hydrophobic potential has no effect on ϕ_0, irrespective of its magnitude (see ϕ_1 and ϕ_2, Fig. 1). However, in reality, the range of the attractive potential does extend beyond $r = a$ (*gray dashed line*, Fig. 1). If the amplitude of the hydrophobic attractive potential increases, the approximation that the electrostatic potential is governed by Eq. 2 close to the surface will become a poor one. The potential maximum will occur further away from the surface, and the value of the barrier will be lowered by the enhanced attractive interaction as can be summarized from Fig. 1. Therefore, increased short-range attraction will lead to larger nanoparticles at the same ionic strength.

MATERIALS AND METHODS

Protein expression and purification

Barstar was expressed and purified as described before (41) and used as such. A$\beta_{1\text{-}40}$ and A$\beta_{1\text{-}42}$ were purchased from rPeptide (Bogart, GA) and were used as such.

Thioflavin-T binding assay

Thioflavin-T (thio-T) is purchased from Sigma Chemicals (St. Louis, MO) and was used as such. The protein samples are prepared in buffers containing 5 μM thio-T. The thio-T fluorescence is recorded in a Fluoromax 3 fluorimeter (SPEX CertiPrep, Stanmore, UK) using an excitation wavelength of 444 nm and an emission wavelength of 488 nm.

Fluorescence correlation spectroscopy (FCS)

Barstar C82A is labeled at Cys^{40} with tetramethyl rhodamine iodoacetate using the protocol supplied by Molecular Probes (Carlsbad, CA). This labeled protein is used at a ratio of 1:1000 to the unlabeled barstar. Rhodamine-labeled A$\beta_{1\text{-}40}$ and A$\beta_{1\text{-}42}$ were purchased from rPeptide. These are used at a ratio of 1:1000 to the unlabeled peptides. FCS measurements are performed in an FCS instrument constructed in-house as described elsewhere (27). The data are analyzed with the MEMFCS fitting routine (27).

RESULTS

Soluble aggregates of A$\beta_{1\text{-}40}$ and A$\beta_{1\text{-}42}$ at pH 7.4

Solutions of each of these peptides were prepared in HEPES buffer at pH 7.4, starting from a stock solution of 230 μM prepared in water at pH 10.5 (the solubility of these peptides are much higher under this condition). The solutions are aged for 2 h. They are then centrifuged at 2000 $\times$ g for 20 min and the supernatant is collected for FCS experiments. The correlation data of these solutions, together with a calibration solution of rhodamine B, is analyzed with the MEMFCS analysis routine in terms of a quasicontinuous distribution of diffusion times (27). The diffusion times are converted into hydrodynamic radii using rhodamine B as a calibrant (hydrodynamic radius = 0.78 nm) (42).The size distribution obtained from the analysis is shown in Fig. 2 (A$\beta_{1\text{-}40}$ is shown as *circles*, whereas A$\beta_{1\text{-}42}$ is shown as *squares*). We see that A$\beta_{1\text{-}40}$ forms soluble aggregates of ~200 nm, but the A$\beta_{1\text{-}42}$ solution does not show any large soluble

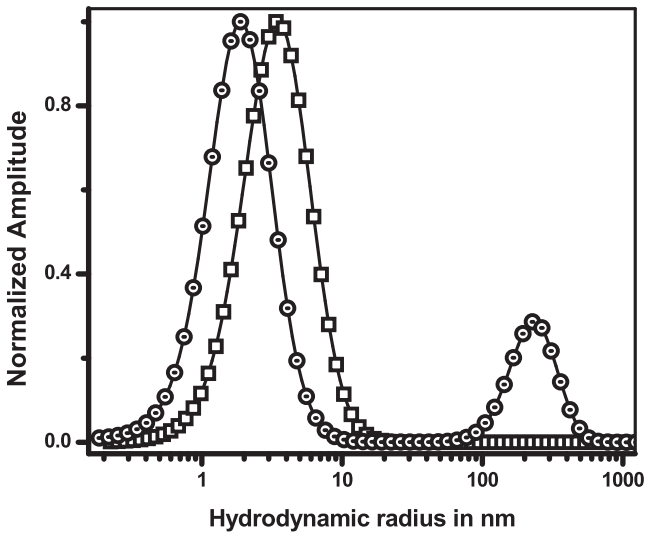

FIGURE 2 Size distribution of A$\beta_{1\text{-}40}$ versus A$\beta_{1\text{-}42}$. Size distribution of A$\beta_{1\text{-}40}$ (*circles*) and A$\beta_{1\text{-}42}$ (*squares*) obtained by MEMFCS analysis of the fluorescence correlation spectroscopy data.

aggregates at this pH. However, the A$\beta_{1\text{-}42}$ solution shows considerable precipitation, indicating that any stable aggregate, if it does exist, is too large to be soluble.

Soluble aggregate formation in A$\beta_{1\text{-}42}$ solution as a function of pH

To investigate whether A$\beta_{1\text{-}42}$ may yield soluble aggregates at a different pH, we prepare the A$\beta_{1\text{-}42}$ solutions of pH 7.4, 9.0, 10.5, and 12.0, and measure the size distribution with FCS. The size distributions obtained from these solutions are shown in Fig. 3 (*open squares*, pH 7.4; *solid stars*, pH 9.0; *open circles*, pH 10.5; and *solid squares*, pH 12.0).

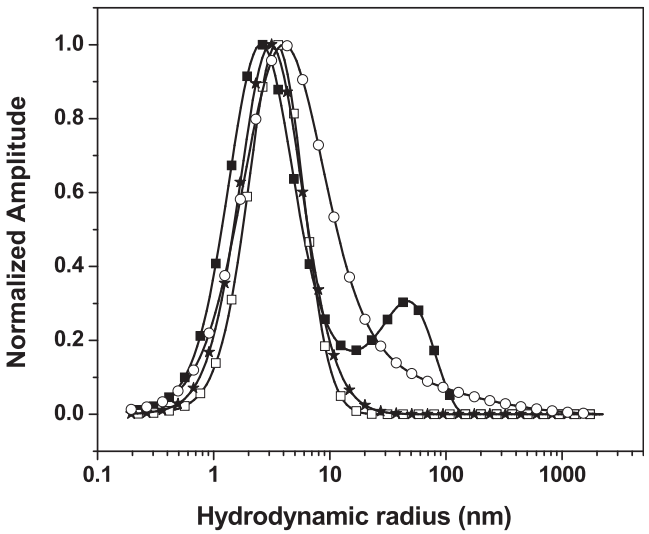

FIGURE 3 Size distribution of A$\beta_{1\text{-}42}$ at different values of pH. The size distributions obtained by MEMFCS analysis of FCS data at pH 7.4 (*open squares*), pH 9.0 (*solid stars*), pH 10.5 (*open circles*), and pH 12.0 (*solid squares*).

We see that the pH 7.4 and the pH 9.0 solutions do not show any tendency to form soluble aggregates. However, the peak gets broader at pH 10.5, indicating the formation of some soluble aggregates. At pH 12.0, the second peak is separate and pronounced, and shows aggregates of size ~50 nm. An increased charge per monomer thus corresponds to a smaller size for the stable nanoparticle.

Soluble aggregates of A$\beta_{1\text{-}42}$ at different ionic strengths

The size determination experiment was then performed in phosphate-buffered solutions at pH 12.0 at six different ionic strengths, i.e., 0, 25, 50, 75, 100, 125, and 150 mM of NaCl (effective approximate ionic strengths of 17, 42, 67, 92, 117, 142, and 167 mM, respectively, taking into account the buffer and other minor salts). The correlation curves are shown in Fig. 4 *a* and the analysis of the curves in terms of the sizes is shown in Fig. 4 *b*. A proper MEMFCS analysis is not possible for all of these curves, as at higher ionic strengths the sizes become too big and bleaching related artifacts cannot be neglected. The analysis in Fig. 4 *b* therefore only considers the $t_{1/2}$ times of the correlation curves, and provides an approximate measure of the sizes of the particles. The correlation curves clearly show a monotonic increase of the characteristic diffusion time (and therefore the average particle size) as the ionic strength increases.

Soluble aggregates of barstar as a function of pH

We prepare 10 μM barstar solutions containing 0.2% of rhodamine-labeled barstar at three different pH values (7.4, 3.5, and 2.0) and incubate these overnight. The solutions are then centrifuged at 2000 $\times$ *g* for 20 min and the supernatants are probed with FCS. Fig. 5 shows the plots of the size distributions obtained at different values of pH (pH 7.4, *squares*; pH 3.5, *circles*; and pH 2.0, *triangles*). Whereas the solution at pH 7.4 shows no large particles, at pH 3.5 we observe soluble aggregates approximately tens of nm in size. At the lower pH of 2.0, the soluble aggregates exhibit a smaller size range (between 10 and 20 nm). Both the lower pH values also show an additional peak at smaller sizes, at ~0.8 nm, which is similar to the hydrodynamic radius of the calibrant rhodamine B, and probably indicate the presence of dissociated dye molecules in the solution.

The degree of hydrophobicity of individual monomers is measured by the binding of the polarity sensitive dye ANS. This is shown in Fig. 5 (*inset*) as a function of pH. ANS binding goes up as the pH is decreased, and peaks at approximately pH 3, but decreases below that. The solution is also probed for thio-T binding, which is supposed to report the formation of the repeated β-sheet structures in a protein (43). There is hardly any change in thio-T fluorescence until the pH reaches ~5.0. However, it then rapidly goes up and becomes maximum at approximately pH 3.5, and then starts going down gradually as the pH is lowered further (data not shown).

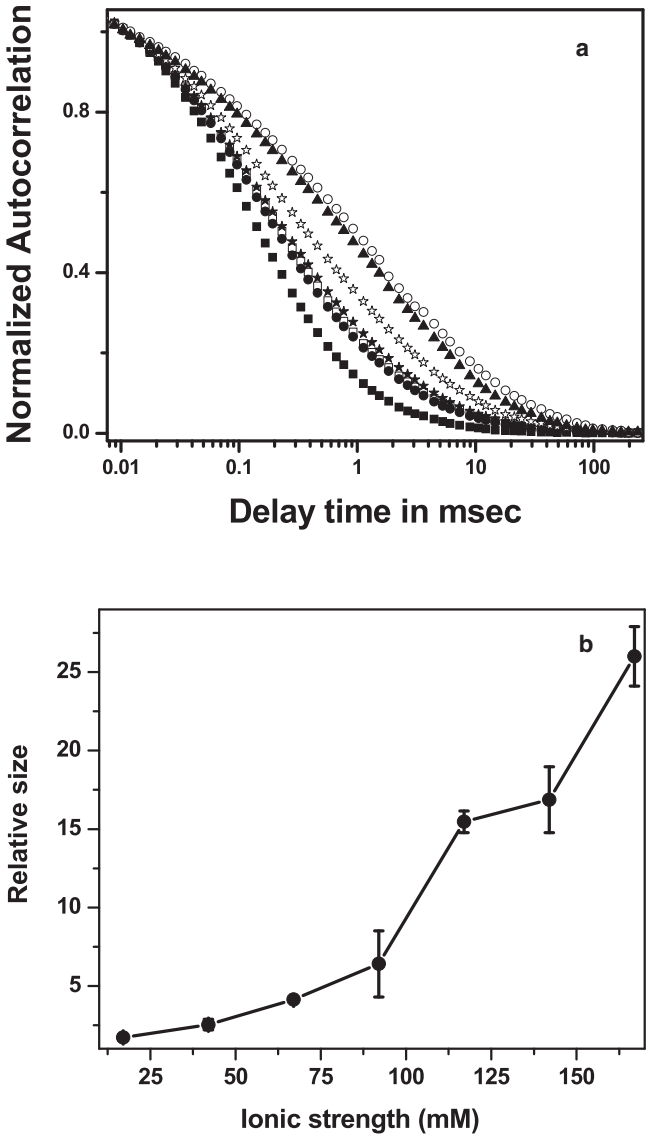

FIGURE 4 Size of nanoparticles as a function of the ionic strength. (*a*) Autocorrelation curves. Ionic strengths of 17 mM (*solid squares*), 42 mM (*open squares*), 67 mM (*solid circles*), 92 mM (*solid stars*), 117 mM (*open stars*), 142 mM (*open circles*), and 167 mM (*solid triangles*), respectively. (*b*) Relative sizes of $A\beta_{1\text{-}42}$ at a function of ionic strength of the solution.

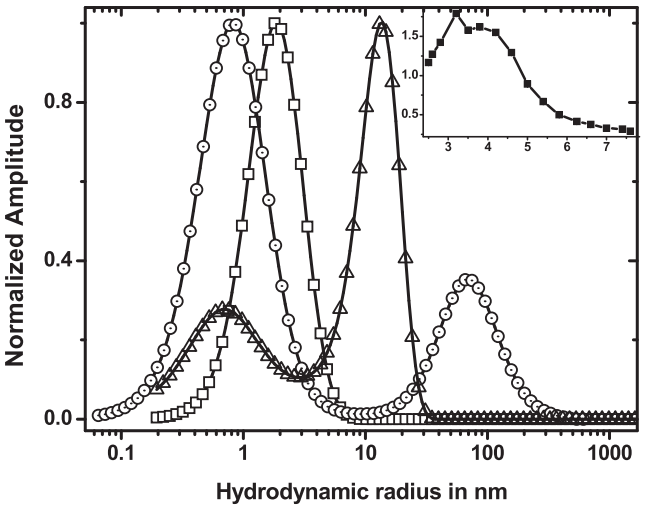

FIGURE 5 Size distribution of barstar as a function of pH. At pH 7.4 (*squares*), pH 3.5 (*circles*), and pH 2.0 (*triangles*) obtained from FCS data. (*Inset*) ANS fluorescence reporting barstar hydrophobicity at several pH values. Abscissa, pH values; and ordinate, ANS fluorescence intensity in arbitrary units.

DISCUSSION

We have used pH, ionic strength, and addition of hydrophobic residues as modulators of the long-range electrostatic repulsion and short-range hydrophobic attraction between the aggregating mono- and oligomers. It is not possible to cleanly partition the contribution of any of these agents to these two factors. However, it is expected that for $A\beta_{1\text{-}40}$, the variation of pH and ionic strength would predominantly affect the electrostatic interaction, whereas the addition of the hydrophobic residues would mostly affect the short-range hydrophobic interaction.

$A\beta_{1\text{-}40}$ at pH 7.4 forms stable soluble aggregates of size at ~200 nm. The hydrophobicity of this peptide can be easily increased by adding hydrophobic residues to the sequence, and $A\beta_{1\text{-}42}$ provides a natural variant of this type. $A\beta_{1\text{-}42}$ shows no large aggregates (Fig. 2). However, the concentration in the supernatant goes down rapidly during incubation (data not shown) and there is visible precipitation from this solution, indicating that aggregation does take place. We infer that the $A\beta_{1\text{-}42}$ nanoparticles do not stabilize at a small enough size to be soluble in aqueous solutions. The effect of increased hydrophobic interaction is consistent with the model represented in Fig. 1 (*gray dashed lines*).

The results change when the pH is altered (Fig. 3). Though the pH 9.0 solution behaves much like the pH 7.4 solution, there is a clear indication of the presence of soluble nanoparticles at pH 10.5. At an even higher pH of 12.0, there is a pronounced peak due to soluble nanoparticles of size ~50 nm. $A\beta_{1\text{-}40}$ has a pI at approximately pH 5.3 (44). However, an analysis of the amino-acid sequence (taking into consideration the individual pK_a values of the amino acids as guidelines) suggests that it is only weakly charged until pH 9, but becomes multipally charged at pH 10.5 and even more strongly charged at pH 12. This indicates that the increase in the charge per monomer caused by the increase in the pH stabilizes the growing particles at smaller sizes. These results agree with the predictions made earlier, and therefore corroborate the overall features of the charged colloid model (23,45). We do note that the possibility of a change of the secondary structure with pH may also contribute to this behavior.

The ionic strength variations provide further tests of the model. A pronounced and monotonous decrease of the particle size is observed as the ionic strength is decreased (Fig. 4 *b*). The screening of the repulsive field is decreased at lower ionic strengths, and therefore the long-range repulsion increases, which tends to stabilize nanoparticles at

a lower size. The observed decrease in the nanoparticle size is consistent with this prediction. Equation 5 would predict that the radius of a stable nanoparticle would vary as $I^{1/2}$, but the observed behavior is clearly superlinear. As discussed in the Theory section, such a behavior is expected for a range of ionic strengths, and possibly suggests a transition from an isotropic pattern of growth to a linear pattern of growth. Johansson et al. (46) have measured the rate of fibril formation as a function of the ionic strength, and they find that the rate increases with the ionic strength. This also is clearly consistent with our results. We note that the hydrophobic effect itself is also a function of the salt concentration (47), increasing with the increase of the ionic strength. However, this effect is typically small at these salt concentrations, and we take these results as further evidence for the charged colloid model.

The barstar results provide further support to our model. This protein is properly folded and completely soluble at a pH of 7.4. As the pH is lowered, two properties change. First, the hydrophobicity of the protein surface increases, as is shown by the increased ANS fluorescence (Fig. 5, *inset*). This is consistent with the protein slowly transforming to its A-form (28,29), which is a molten globulelike state. However, this reaches a peak at 3.5, and decreases upon further decrease of the pH, as the molten globule state is increasingly replaced by a random coil-like state. Additionally, the monomers get increasingly charged at lower pH values, as it goes further away from the pI of ~5. The model would therefore predict possible stable nanoparticles at pH~3.5 and smaller nanoparticles at lower pH values. This is indeed observed. The thio-T binding data further shows the amyloidlike nature of the nanoparticles at these pH values. We infer that the soluble amyloid aggregates of a larger size range are stabilized when the protein monomers are more hydrophobic and less charged.

The validity of the charge colloid model suggests that a molecular agent that can increase the short-range attraction (its strength and /or its range; see Fig. 1, *gray dashed lines*) can be a very effective agent for destabilizing the nanoparticles. It has been suggested that Zn^{2+} can potentially cross-link multiple Aβ monomers (48). A cross-linker would in effect increase the short-range attraction between Aβ monomers. It would also increase the range of interaction close to that of the length of a single Aβ molecule, which is approximately the Debye screening length. This should push the nanoparticles to higher sizes and precipitate them, leading to a lowering of Aβ toxicity. This has indeed been observed recently (7).

Overall, the evidence from the proteins and peptides examined by us, and other preexisting data, strongly suggest that the charged colloid model correctly describes the size and the stability of the soluble aggregates of amyloid protein. The model therefore provides a simple logical framework for designing agents (e.g., Aβ cross-linkers) that can modulate the stability of protein nanoparticles.

The barstar protein was expressed and purified using clones and facilities available in the laboratory of Jayant Udgaonkar. We thank Deepak Dhar for fruitful discussions on the theory of aggregation of charged colloids.

REFERENCES

1. Selkoe, D. J. 1991. The molecular pathology of Alzheimer's disease. *Neuron*. 6:487–498.
2. Selkoe, D. J. 2001. Alzheimer's disease: genes, proteins, and therapy. *Physiol. Rev*. 81:741–766.
3. Teplow, D. B. 1998. Structural and kinetic features of amyloid β-protein fibrillogenesis. *Amyloid*. 5:121–142.
4. Irvine, G. B., O. M. El-Agnaf, G. M. Shankar, and D. M. Walsh. 2008. Protein aggregation in the brain: the molecular basis for Alzheimer's and Parkinson's diseases. *Mol. Med*. 14:451–464.
5. Chiti, F., and C. M. Dobson. 2006. Protein misfolding: functional amyloid and human disease. *Annu. Rev. Biochem*. 75:333–366.
6. Selkoe, D. J. 2008. Soluble oligomers of the amyloid β-protein impair synaptic plasticity and behavior. *Behav. Brain Res*. 192:106–113.
7. Garai, K., B. Sahoo, S. K. Kaushalya, R. Desai, and S. Maiti. 2007. Zinc lowers amyloid β-toxicity by selectively precipitating aggregation intermediates. *Biochemistry*. 46:10655–10663.
8. Glabe, C. G., and R. Kayed. 2006. Common structure and toxic function of amyloid oligomers implies a common mechanism of pathogenesis. *Neurology*. 66:S74–S78.
9. Selkoe, D. J. 2008. Biochemistry and molecular biology of amyloid β-protein and the mechanism of Alzheimer's disease. *Handbook Clin. Neurol*. 89:245–260.
10. Glabe, C. G. 2008. Structural classification of toxic amyloid oligomers. *J. Biol. Chem*. 283:29639–29643.
11. Walsh, D. M., A. Lomakin, G. B. Benedek, M. M. Condron, and D. B. Teplow. 1997. Amyloid β-protein fibrillogenesis. Detection of a protofibrillar intermediate. *J. Biol. Chem*. 272:22364–22372.
12. Walsh, D. M., D. M. Hartley, Y. Kusumoto, Y. Fezoui, M. M. Condron, et al. 1999. Amyloid β-protein fibrillogenesis. Structure and biological activity of protofibrillar intermediates. *J. Biol. Chem*. 274:25945–25952.
13. Garai, K., P. Sengupta, B. Sahoo, and S. Maiti. 2006. Selective destabilization of soluble amyloid β-oligomers by divalent metal ions. *Biochem. Biophys. Res. Commun*. 345:210–215.
14. Perutz, M. F., and A. H. Windle. 2001. Cause of neural death in neurodegenerative diseases attributable to expansion of glutamine repeats. *Nature*. 412:143–144.
15. Ferrone, F. A. 2006. Nucleation: the connections between equilibrium and kinetic behavior. *Methods Enzymol*. 412:285–299.
16. Sengupta, P., K. Garai, B. Sahoo, Y. Shi, D. J. Callaway, et al. 2003. The amyloid β-peptide ($A\beta_{1\text{-}40}$) is thermodynamically soluble at physiological concentrations. *Biochemistry*. 42:10506–10513.
17. Lomakin, A., D. S. Chung, G. B. Benedek, D. A. Kirschner, and D. B. Teplow. 1996. On the nucleation and growth of amyloid-protein fibrils: detection of nuclei and quantitation of rate constants. *Proc. Natl. Acad. Sci. USA*. 93:1125–1129.
18. Jarrett, J. T., E. P. Berger, and P. T. Lansbury, Jr. 1993. The carboxy terminus of the β-amyloid protein is critical for the seeding of amyloid formation: implications for the pathogenesis of Alzheimer's disease. *Biochemistry*. 32:4693–4697.
19. Garai, K., B. Sahoo, P. Sengupta, and S. Maiti. 2008. Quasihomogeneous nucleation of amyloid-β yields numerical bounds for the critical radius, the surface tension, and the free energy barrier for nucleus formation. *J. Chem. Phys*. 128:045102–045107.
20. Hortschansky, P., V. Schroeckh, T. Christopeit, G. Zandomeneghi, and M. Fandrich. 2005. The aggregation kinetics of Alzheimer's β-amyloid peptide is controlled by stochastic nucleation. *Protein Sci*. 14:1753–1759.

21. Groenewold, J., and W. K. Kegel. 2001. Anomalously large equilibrium clusters of colloids. *J. Phys. Chem. B*. 105:11702–11709.

22. Sciortino, F., S. Mossa, E. Zaccarelli, and P. Tartaglia. 2004. Equilibrium cluster phases and low-density arrested disordered states: the role of short-range attraction and long-range repulsion. *Phys. Rev. Lett*. 93:055701.

23. Stradner, A., H. Sedgwick, F. Cardinaux, W. C. Poon, S. U. Egelhaaf, et al. 2004. Equilibrium cluster formation in concentrated protein solutions and colloids. *Nature*. 432:492–495.

24. Shukla, A., E. Mylonas, E. Di Cola, S. Finet, P. Timmins, et al. 2008. Absence of equilibrium cluster phase in concentrated lysozyme solutions. *Proc. Natl. Acad. Sci. USA*. 105:5075–5080.

25. Maiti, S., U. Haupts, and W. W. Webb. 1997. Fluorescence correlation spectroscopy: diagnostics for sparse molecules. *Proc. Natl. Acad. Sci. USA*. 94:11753–11757.

26. Haupts, U., S. Maiti, P. Schwille, and W. W. Webb. 1998. Dynamics of fluorescence fluctuations in green fluorescent protein observed by fluorescence correlation spectroscopy. *Proc. Natl. Acad. Sci. USA*. 95:13573–13578.

27. Sengupta, P., K. Garai, J. Balaji, N. Periasamy, and S. Maiti. 2003. Measuring size distribution in highly heterogeneous systems with fluorescence correlation spectroscopy. *Biophys. J*. 84:1977–1984.

28. Gast, K., A. J. Modler, H. Damaschun, R. Krober, G. Lutsch, et al. 2003. Effect of environmental conditions on aggregation and fibril formation of barstar. *Eur. Biophys. J*. 32:710–723.

29. Kumar, S., S. K. Mohanty, and J. B. Udgaonkar. 2007. Mechanism of formation of amyloid protofibrils of barstar from soluble oligomers: evidence for multiple steps and lateral association coupled to conformational conversion. *J. Mol. Biol*. 367:1186–1204.

30. Mukhopadhyay, S., P. K. Nayak, J. B. Udgaonkar, and G. Krishnamoorthy. 2006. Characterization of the formation of amyloid protofibrils from barstar by mapping residue-specific fluorescence dynamics. *J. Mol. Biol*. 358:935–942.

31. Juneja, J., N. S. Bhavesh, J. B. Udgaonkar, and R. V. Hosur. 2002. NMR identification and characterization of the flexible regions in the 160 kDa molten globule-like aggregate of barstar at low pH. *Biochemistry*. 41:9885–9899.

32. Wintrode, P. L., Y. V. Griko, and P. L. Privalov. 1995. Structural energetics of barstar studied by differential scanning microcalorimetry. *Protein Sci*. 4:1528–1534.

33. Ermakova, E. 2007. Brownian dynamics simulation of the competitive reactions: binase dimerization and the association of binase and barstar. *Biophys. Chem*. 130:26–31.

34. Magde, D., E. Elson, and W. W. Webb. 1974. Fluorescence correlation spectroscopy. II. An experimental realization. *Biopolymers*. 13:29–61.

35. Elliot, L., and D. M. Elson. 1974. Fluorescence correlation spectroscopy. I. Conceptual basis and theory. *Biopolymers*. 13:1–27.

36. Magde, D., E. Elson, and W. W. Webb. 1972. Thermodynamic fluctuations in a reacting system—measurement by fluorescence correlation spectroscopy. *Phys. Rev. Lett*. 29:705.

37. Meyer, E. E., K. J. Rosenberg, and J. Israelachvili. 2006. Recent progress in understanding hydrophobic interactions. *Proc. Natl. Acad. Sci. USA*. 103:15739–15746.

38. Lum, K., D. Chandler, and J. D. Weeks. 1999. Hydrophobicity at small and large length scales. *J. Phys. Chem. B*. 103:4570–4577.

39. Rice, S. A., and M. Nagasawa. 1961. Polyelectrolyte Solutions. Academic Press, London, UK.

40. Levin, Y. 2002. Electrostatic correlations: from plasma to biology. *Rep. Prog. Phys*. 65:1577–1632.

41. Khurana, R., and J. B. Udgaonkar. 1994. Equilibrium unfolding studies of barstar: evidence for an alternative conformation which resembles a molten globule. *Biochemistry*. 33:106–115.

42. Rani, S. A., B. Pitts, and P. S. Stewart. 2005. Rapid diffusion of fluorescent tracers into *Staphylococcus epidermidis* biofilms visualized by time lapse microscopy. *Antimicrob. Agents Chemother*. 49:728–732.

43. LeVine, 3rd, H. 1999. Quantification of β-sheet amyloid fibril structures with thioflavin T. *Methods Enzymol*. 309:274–284.

44. Burdick, D., B. Soreghan, M. Kwon, J. Kosmoski, M. Knauer, et al. 1992. Assembly and aggregation properties of synthetic Alzheimer's A4/β amyloid peptide analogs. *J. Biol. Chem*. 267:546–554.

45. Foffi, G., G. D. McCullagh, A. Lawlor, E. Zaccarelli, K. A. Dawson, et al. 2002. Phase equilibria and glass transition in colloidal systems with short-ranged attractive interactions: application to protein crystallization. *Phys. Rev. E Stat. Nonlin. Soft Matter Phys*. 65:17.

46. Johansson, A. S., F. Berglind-Dehlin, G. Karlsson, K. Edwards, P. Gellerfors, et al. 2006. Physiochemical characterization of the Alzheimer's disease-related peptides A$\beta_{1\text{-}42}$Arctic and A$\beta_{1\text{-}42}$wt. *FEBS J*. 273:2618–2630.

47. Baldwin, R. L. 1996. How Hofmeister ion interactions affect protein stability. *Biophys. J*. 71:2056–2063.

48. Dong, J., J. E. Shokes, R. A. Scott, and D. G. Lynn. 2006. Modulating amyloid self-assembly and fibril morphology with Zn^{II}. *J. Am. Chem. Soc*. 128:3540–3542.